

Wide-field magnetometry with nitrogen-vacancy centers in randomly oriented micro-diamonds

S. Sengottuvel,^{1,*} M. Mrózek,¹ M. Sawczak,² M. J. Głowacki,³ M. Ficek,³ W. Gawlik,¹ and A. M. Wojciechowski^{1,1}

¹*Institute of Physics, Jagiellonian University, 11 Łojasiewicza St., 30-348 Kraków, Poland*

²*Szewalski Institute of Fluid-Flow Machinery, Polish Academy of Sciences, 14 Fiszerza St., 80-231 Gdansk, Poland*

³*Gdansk University of Technology, 11/12 G. Narutowicza St., 80-233 Gdansk, Poland*

(Dated: June 14, 2022)

Magnetometry with nitrogen-vacancy color centers in diamond has gained significant interest among researchers in recent years. Absolute knowledge of the three-dimensional orientation of the magnetic field is necessary for many applications. Conventional magnetometry measurements are usually performed with NV ensembles in a bulk diamond with a thin NV layer or a scanning probe in the form of a diamond tip, which requires a smooth sample surface and proximity of the probing device, often limiting the sensing capabilities. Here, we present a method for determining the three-dimensional orientation of the magnetic field vector relative to the diamond crystal lattice. We demonstrate that NV centers in arbitrarily oriented submicrometer-sized diamond powder deposited on a planar surface can be used for sensing the magnetic field. Our work can be extended to irregular surfaces, which shows a promising path for nanodiamond-based photonic sensors.

I. INTRODUCTION

Mapping the magnetic field vector and its orientation with micro- and nanoscale resolution is crucial for many applications [1, 2]. Various types of magnetic sensors have been developed on a variety of platforms over the past decades such as superconducting quantum interference devices (SQUIDS) [3], fluxgate devices [4], and optically pumped magnetometers using alkali atom vapor cells [5, 6] that offer the measurement of magnetic fields at high sensitivities. Generally, these sensors are limited in their spatial and sensitivity resolution due to their finite size, probing distance to the sample, and the operating environment. In recent years, the negatively charged nitrogen-vacancy (NV⁻) center (hereafter NV) in diamond has emerged as one of the most promising tools for magnetic sensing and imaging. At room temperature for large NV ensembles with sensitivity reaching the pT/ $\sqrt{\text{Hz}}$ level [7, 8] and high spatial resolution with single NV centers [9]. Numerous experimental studies with NV centers were carried out to detect electric fields [10], temperature [11], pressure [12], and magnetic fields [13–15] with spatial resolution down to the nanoscale.

The spectacular advent of NV sensors is based on the very attractive optical and spin properties of NV color centers in diamond. The NV defect in a diamond carbon lattice acts as a single isolated atom-like system consisting of a substitutional nitrogen atom with an adjacent vacancy. The electronic ground state of the NV center is a triplet state $S = 1$ with spin sublevels $m_s = 0$ and $m_s = \pm 1$ [16]. The spin sublevels are degenerate but are split from the spin state $m_s = 0$ by roughly $D = 2.87$ GHz [17] at zero magnetic field and room temperature. The ground-level spin states of NV center can be manipulated by microwaves and initialized and read out optically owing to the state-dependent fluorescence [18]. When an external magnetic field is applied, the degeneracy

between the $m_s = \pm 1$ states is lifted and these states split proportionally to the applied field strength (~ 56 MHz/mT at low magnetic fields). Magnetic field detection with NV centers is performed by quantitatively measuring the Zeeman shifts [19] using the optically detected magnetic resonance (ODMR) technique [20]. Because of the C_{3v} symmetry of the NV defect, the center's quantization axis can take one of the four possible orientations in the diamond lattice. Depending on the orientation of the magnetic field relative to the four crystallographic NV axes, the ODMR signal from the NV ensembles will exhibit between one and four pairs of resonance splittings between the states $m_s = -1$ and $m_s = +1$. When an applied magnetic field is oriented arbitrarily, each of the four NV crystallographic axes will sense a different field strength. In this scenario, the NV ensembles will exhibit four pairs of resonance splittings. Taking advantage of the position and angle dependence of the NV center quantization axis on the applied magnetic field and measuring the exact frequency of these resonance pairs, we can reconstruct the magnetic field vector in all spatial coordinates [21, 22].

In this experimental study, we propose a simple and inexpensive wide-field magnetometer using NV ensembles in diamond. Moreover, we performed the magnetometer's applicability by spatially mapping the magnetic field distribution from a DC field in a straight current-carrying wire placed in near proximity to the diamond sample. Our approach is an extension of the work reported in [23], where a narrow NV diamond slab has been used to measure the magnetic field. In this work and as a proof-of-concept experiment, we probed the NV centers in randomly oriented 1- μm -sized microdiamonds that were deposited on a planar glass substrate. We measured the ODMR signals in such randomly oriented diamonds and used them to perform scalar and vector magnetometry relative to the diamond lattice. In gen-

eral, this method can be extended to micro- and nanodiamonds deposited on any material surface. The results obtained in this work show a promising path to low-cost micro- and nanodiamond-based photonic sensors.

II. MATERIALS AND METHODS

A. Diamond Sample

Our main criteria for preparing a suitable diamond sample for magnetic sensing were sample volume, high concentration of NV centers, and proximity of NV centers to the surface. Such a diamond sample could be prepared by the laser ablation process in diamond micro or nanoparticles, the so-called Matrix-Assisted Pulsed Laser Evaporation (MAPLE) [24] deposition technique. The base target for laser ablation was prepared by suspending the microdiamond powder in deionized water. The suspension was solidified at cryogenic temperature (90-100 K) and served as a target in the MAPLE process. The deposition was carried out under vacuum conditions (10^{-5} mbar). Thin films were made on glass coverslips (1×1 cm²) mounted at a distance of 15 mm from the target surface and preheated at temperatures in the range of 293-323 K to prevent condensation of the solvent originating from droplets of the molten target.

B. The Experimental Setup

The wide-field imaging magnetometry with NV centers in arbitrarily oriented diamond crystals was performed using the optical microscopy setup shown in Fig. 1a. The wide-field microscopy setup consists primarily of a few optical elements, a microwave (MW) subsystem, and an imaging subsystem. The microwave subsystem comprises a microwave structure Fig. 1b consists of two straight copper striplines (100- μ m wide) fabricated on a PCB board with a separation of 350 μ m [25] between them. One of the striplines transmits the microwave signal from a signal generator (Agilent N9310A). A Mini-Circuits ZRL-3500+ power amplifier is connected after the MW generator to amplify the microwave signal. The typical gain of the MW power amplifier is +17 dB at 2800 MHz. This microwave system is used to manipulate the ground-level spin states of the NV centers. The second stripline conducts a DC current that creates a local magnetic field to be characterized together with the bias field. MW and DC currents are applied simultaneously. The optical and imaging subsystem consists of a laser, dichroic mirror, lenses, microscope objective, and a camera for NV fluorescence imaging. The NV center ground-level spin triplet states were optically pumped to the excited state by a 530 nm green LED light source (Thorlabs M530L4). The pump beam was collimated by

an aspheric condenser lens of focal length 50 mm and deflected by a dichroic mirror on the back focal plane of the 40X Olympus microscope objective with a numerical aperture of 0.65. The pump beam focused by the objective illuminates the top surface of the diamond sample over a field of view (FOV) of 308 x 246 μ m. Red fluorescence emitted from the NV centers was collected using the same microscope objective used to deliver the pump beam. Additional optical filters and lenses ensure that the emitted red fluorescence was properly focused and imaged by an IDS UI-3240 CP camera equipped with a CMOS sensor with 12 bit depth. A small bias magnetic field (3.2 mT) from a neodymium permanent magnet is applied to lift the degeneracy between the states of $m_s = \pm 1$.

C. Wide-field ODMR Imaging

The imaging scheme in the described wide-field diamond magnetometer works as follows; the excitation of ground-state spins is achieved by continuously illuminating the diamond sample with a 70 mW pump beam (beam power measured at the output side of the microscope objective). Under continuous light illumination, the microwave frequency is swept around the $m_s = \pm 1$ transition resonance frequency of 2.87 GHz with a step resolution of 1.5 MHz. The red fluorescence signal emitted from the diamond sample was then recorded by taking a single snapshot of the sample FOV for each MW frequency and stored in the computer. This results in volumetric image data with rows and columns of pixels forming 2D slices with N frames that form the volume. The ODMR signals were simultaneously imaged from all the fluorescent diamond spots over the entire field of view of the objective in one shot. Such wide-field imaging is considered to be faster and more efficient than confocal scanning using an NV probe on an AFM [26], which typically requires hours of measurement time to scan the whole sample area.

III. RESULTS

A. Multi-Pixel Extraction of the ODMR Spectrum

In order to extract the ODMR signals from the volumetric image data, we employ an internally developed MATLAB algorithm [27]. Bright fluorescent diamond spots were first identified from a single frame of the image data. Each identified diamond spot is then characterized by its XY position, pixel region (in our case, an elliptical area with its semimajor and minor axes) and the orientation in the XY plane. In addition, spots are sequentially numbered for future identification and association with the corresponding ODMR spectrum.

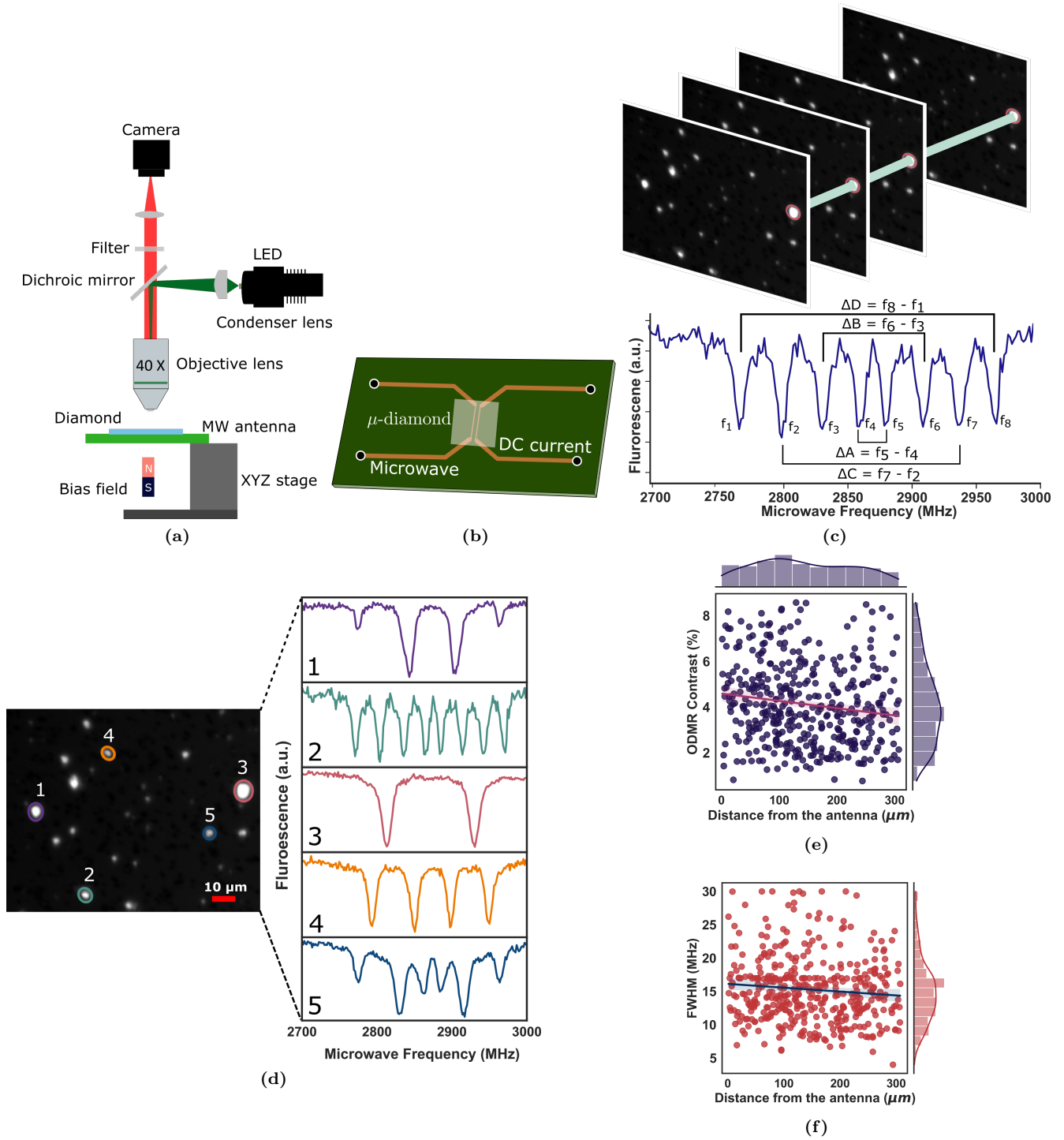


Fig. 1. a) Schematic of the wide-field diamond magnetometer used for the described magnetic imaging. b) Layout of the microwave and current wire structure printed on a PCB with a diamond sample in the center. c) Scheme of the ODMR imaging method in which the camera captures an image for a given MW frequency. A total of N frames are obtained by sweeping the microwave frequency around 2.87 GHz. The ODMR signal is obtained by averaging n pixels over the pixel region. The original volumetric data contain the ODMR spectrum for each diamond spot. (d) Example image frame with randomly oriented diamond crystals seen in the field of view of the microscope objective and the corresponding ODMR spectra extracted from the image data for five different diamond spots. Each of the diamond crystals is oriented at different angles with respect to the magnetic field direction. (e-f) ODMR contrast and FWHM of all diamond spots as a function of the distance from the MW antenna. The side panels show the histogram plotted with the kernel density estimation.

The ODMR signals are then obtained in a straightforward manner: for a given diamond spot, the ODMR spectrum is extracted by averaging the pixel values within the pixel region. The mean pixel intensity for a single spot obtained from one frame gives a single data point on the ODMR spectrum. The procedure is then repeated for all frames, resulting in a complete ODMR spectrum as shown in Fig. 1c. An elliptical pixel region is adapted for averaging the pixels due to the random orientation of the diamond aggregates when they are deposited on a planar surface.

The pixel region is predetermined while the algorithm identifies the diamond spots, and the size of the region depends on the size of the diamond aggregate. The whole data analysis procedure is fully automated from the initial reading of the volumetric data, identifying the diamond spots, extraction of ODMR spectra, fitting the resonance peaks, and finally estimating the magnetic field intensities, and does not require visual analysis or human intervention. Shown in Fig. 1d is an example of ODMR spectra from five arbitrarily oriented diamond spots extracted using the automated algorithm. Each of the diamond spots exhibits a different number of splittings as a result of random crystallographic orientation to the magnetic field direction. The ODMR contrast and the FWHM (with each axis side showing the kernel density estimation overlaid on marginal histograms to visualize the distribution of each variable) for all diamond spots in the field of view are shown in Figs. 1e and 1f, respectively. ODMR imaging was performed in a zero bias field and zero current in the wire. The contrast of ODMR varied between 1% and 8% depending on the number of NV centers in a diamond spot, the size of the diamond aggregate, and the microwave power at the location of the diamond spot. The contrast decreases as the distance from the antenna increases. The average FWHM value of the linear fit is estimated to be 16 MHz. The larger linewidth is caused by a high microwave power that causes power broadening of the ODMR spectrum.

B. Effect of pixel region size and positional drift

An important effect to consider in the automated data analysis procedure is the effect of pixel region size and positional drift of diamond spots, both of which can adversely affect the ODMR contrast and linewidth of the extracted ODMR spectrum from the image data, which could lead to inaccurate estimation of the magnetic field values. Hence, it is important to correctly estimate the pixel region with the appropriate size to average the pixels. Therefore, it is necessary to validate the predetermined pixel region size by the algorithm so that the extracted ODMR spectrum has the maximum contrast and minimal FWHM. We performed an analysis on several diamond spots with various pixel region sizes (see Fig. 2a)

and found that for most of the diamond spots, the pixel region estimated by the algorithm is accurate enough to obtain the maximum ODMR contrast and minimal linewidth as shown in Figs. 2b and 2c respectively. During magnetic imaging measurements, the XY position of an individual diamond spot often moves, typically by 1-2 pixels, between successive frames and repeated scans. This positional drift is attributed to the thermal instabilities of the glass substrate that hosts the diamond crystals and is caused by the heat from the microwave antenna and the current wire at higher current intensities. In addition, the continuous illumination of the laser adds up to sample heating. Positional drifts between frames are corrected by correctly identifying the same fluorescent spot in successive frames by finding the minimum distance $d(p, q)^2 = (q_1^2 - p_1^2) + (q_2^2 - p_2^2)$ between two diamond spots p and q and then updating the XY coordinates for each frame while keeping the size of the pixel region constant. With this distance minimization approach, we eliminate the problems associated with image translation and rotation.

C. Estimation of magnetic field from a current-carrying wire

Due to the random orientation of the diamond crystals, the four crystallographic axes of the NVs are also randomly oriented with respect to the applied bias field direction. This implies that for a given set of N diamond spots, a certain population is observed to have four discernible pairs of ODMR resonances, while some population exhibits ODMR resonances associated with specific crystallographic directions such as $\{111\}$, $\{100\}$ and $\{110\}$ families. The different ODMR spectrum obtained from a single measurement of the microwave scan shows the arbitrariness in the orientation of the diamond crystals with respect to the magnetic field direction. The resonance spectrum is fitted to a sum of eight Lorentzians using the Levenberg-Marquardt (LM) algorithm to obtain the exact resonance frequencies. The LM algorithm requires initial guesses for the fitting function to work that are not too arbitrary from the final result. The initial fit parameters are predetermined fully by the automated script taking advantage of the MATLAB inbuilt functions. For estimating the magnetic field strength, only the diamond spots that exhibit four pairs of resonances were taken into account.

$$f(v) = 1 - \sum_{i=1 \dots 8} C_i \left(\frac{\gamma^2}{4(x_i - x_c)^2 + \gamma^2} \right) \quad (1)$$

where C_i is the contrast, γ is the full width at half-maximum (equal for all resonances), and x_c is the central position of a single resonance. The precise parameters obtained from the fit were used to determine the bias magnetic field strength and the field generated by the

current wire. The ^{14}N hyperfine splitting could not be resolved in our measurement using our wide-field setup. Moreover, the four pairs of resonances were not well

resolved because of the limitation in the generation of higher radio frequencies of our MW generator, although the magnetic resonance peaks are clearly visible with a few MHz separation between each peak.

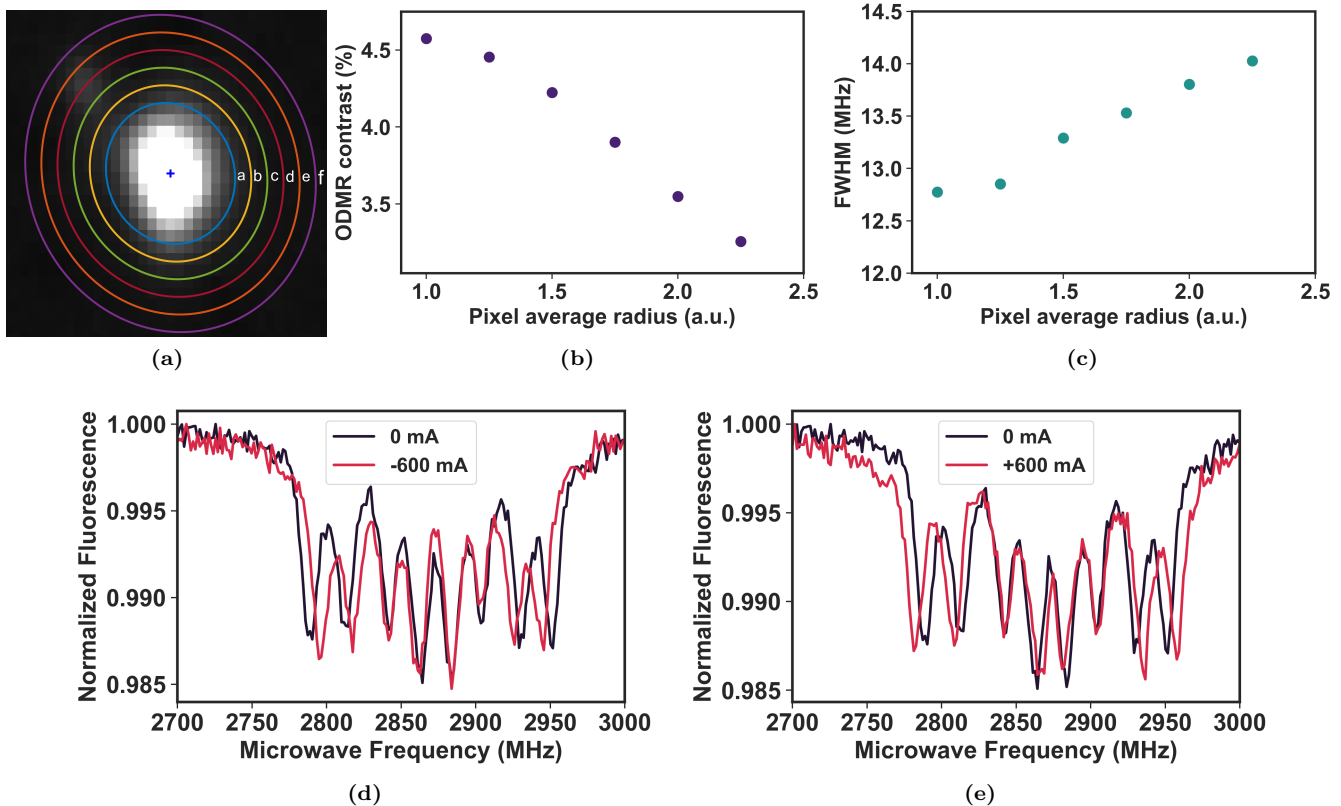


Fig. 2. (a) The fluorescent diamond aggregate with different binning radius encircled in different colors. (b) ODMR contrast for different binning area. (c) FWHM for different binning area. (d) ODMR resonance spectra in presence of a bias field at zero current (black) and 600 mA (red) in the current-carrying wire. (e) same as (d) with the direction of current reversed in the current-carrying wire.

The diamond lattice coordinate frame (i,j,k) is chosen such that the unit vectors u_a, u_b, u_c, u_d have the following coordinates: $u_a = \frac{1}{\sqrt{3}}(1, 1, 1)$, $u_b = \frac{1}{\sqrt{3}}(-1, -1, 1)$, $u_c = \frac{1}{\sqrt{3}}(-1, 1, -1)$, $u_d = \frac{1}{\sqrt{3}}(1, -1, -1)$. The magnetic field components B_i, B_j, B_k to be measured are given by the magnetic field projection m_a, m_b, m_c, m_d on the four NV quantization axes, respectively. Thus, we obtain the following.

$$\begin{aligned} B_i &= \frac{\sqrt{3}}{4}(-m_a + m_b + m_c + m_d) \\ B_j &= \frac{\sqrt{3}}{4}(-m_a + m_b + m_c + m_d) \\ B_k &= \frac{\sqrt{3}}{4}(-m_a + m_b + m_c + m_d). \end{aligned} \quad (2)$$

Finally, the norm of the magnetic field vector \vec{B} gives the total magnetic field strength sensed by the NV ensembles,

$$\text{given as } |B| = \sqrt{B_i^2 + B_j^2 + B_k^2}.$$

In a first set of experiments, with properly optimized experimental settings (laser power output, bias field, and MW frequency bandwidth), we performed the ODMR magnetic imaging in the presence of a bias field and with zero current. We observed a linear dependence of resonance splittings as a function of the magnetic field, and the bias-field strength is determined using the Eq. 2. The estimated value of the bias field from the measurement is 3.2 mT. Once the bias field is estimated, we repeat the ODMR measurement for different current intensities for the same FOV of the diamond sample. A DC current in the range of -600 mA to 600 mA is applied to other strip line of MW structure that was placed directly below the diamond sample so that the current wire lies in the x direction. The MW structure is oriented so that each of the strip lines occupies the start and end of the objective FOV. The NV centers sense both the magnetic

field generated by the current wire and the applied bias field from the permanent magnet, and the field is given by $\vec{B}_{NV} = \vec{B}_{bias} + \vec{B}_I$. Figures 2d and 2e show the ODMR plots obtained from a single diamond spot for

current values -600 mA and 600 mA, respectively, overlaid with 0 mA ODMR spectrum. It is evident from the plots that the total magnetic field intensity sensed by NV ensembles is slightly higher for 600 mA and is lower when the direction of the current is reversed for the same current value.

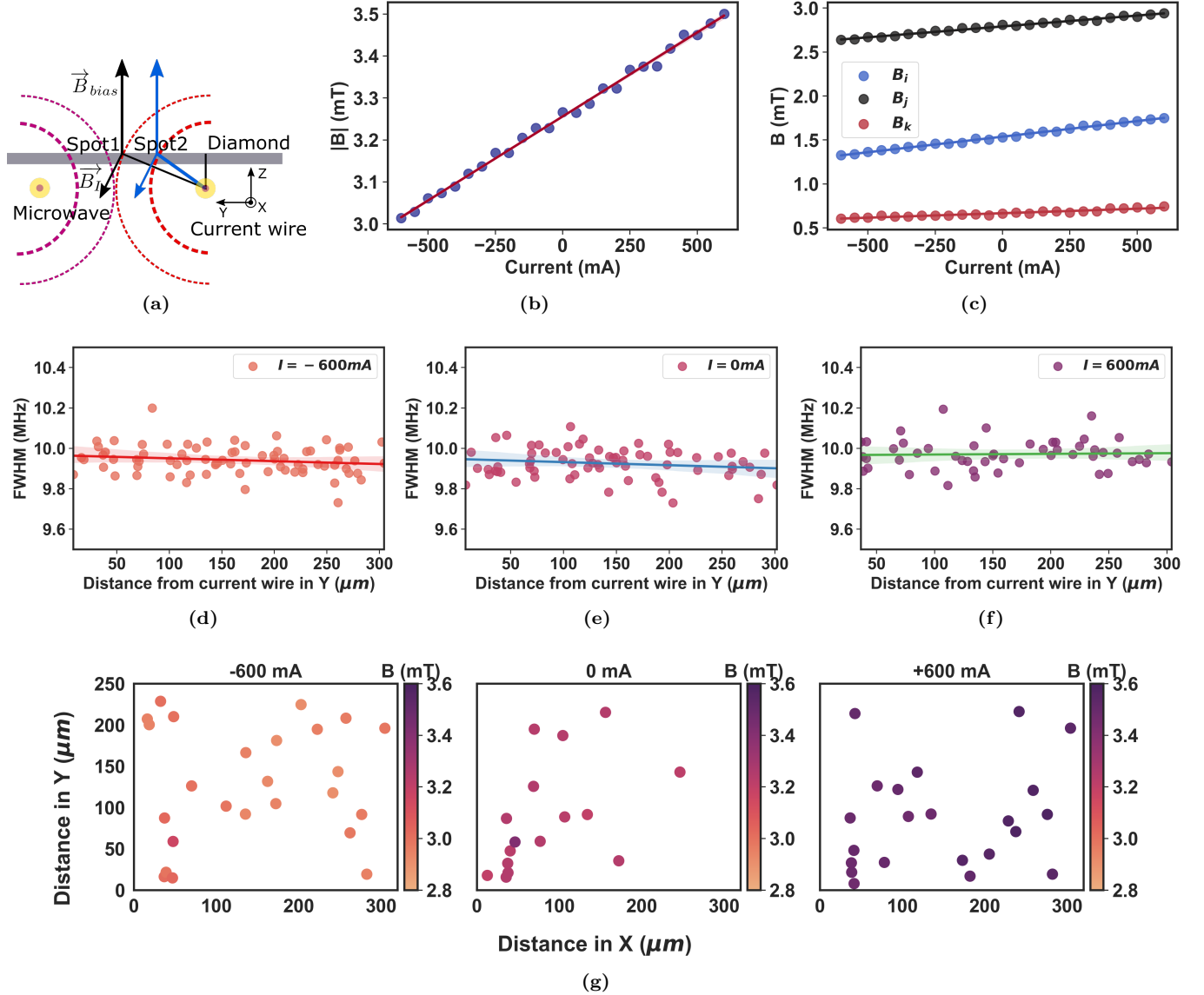


Fig. 3. (a) Scheme of the diamond sample and current wire with magnetic field lines (dashed magenta lines). B_I and B_{bias} denote the direction of the magnetic field vector for bias and current wire, respectively. (b) The three individual field components measured from a single diamond spot. (c) The total magnetic field value is plotted against different current intensities for a single diamond spot. (d-f). FWHM extracted from the Lorentzian fit for arbitrarily oriented diamond spots for current values -600 mA, 0 mA and 600 mA respectively. (g) Map of magnetic field strength for current set at -600 mA, 0 and 600 mA with the field strength indicated in the colorbar. The scatter points indicate the XY position of the randomly oriented micro-diamond crystal in the field-of-view. The current wire is situated to the right of the field map.

The current wire produces an ortho-radial magnetic field in the yz plane. Depending on the direction of the

current flow in the wire, \vec{B}_I adds or subtracts from the field \vec{B}_{bias} . The diamond sensor with the NV centers

was deposited on a glass cover slip with a thickness of 1.7 mm which introduces a small height in the z direction, as shown in the schematic Fig. 3a. The magnetic field sensed by the NV no longer decreases by $1/r$ from the center of the current wire. The additional small height in the z -direction introduces an angle dependence to the resultant magnetic field vector. The diamond spots (spot1 and spot2) sense different magnetic field strengths depending on their position in the XY plane. Due to the non-circular shape of the current wire, the angle dependence of \vec{B}_I could not be accurately estimated. The total magnetic field and components of the magnetic field in the NV diamond frame for a single diamond spot are shown in Figs. 3b and 3c, respectively. It is clearly seen that the magnetic field sensed by the NV centers increases with the increase in the current intensities and decreases when the current is reversed. Additionally, we measured the FWHM for all the diamond spots in Figs. (3d-3f) that were arbitrarily oriented to the magnetic field and found its value to be 10 ± 0.3 MHz. No significant broadening of the ODMR peaks was observed even at higher currents, and the FWHM of the diamond spots at 600 mA was consistent with the FWHM at 0 mA. This suggests that our arbitrarily oriented diamond sensor can work in a wide range, allowing us to detect smaller field fluctuations. The spatial magnetic field distribution estimated using NV centers in multiple diamond spots for three different current values -600 mA, 0 mA and 600 mA are shown in Fig. 3g.

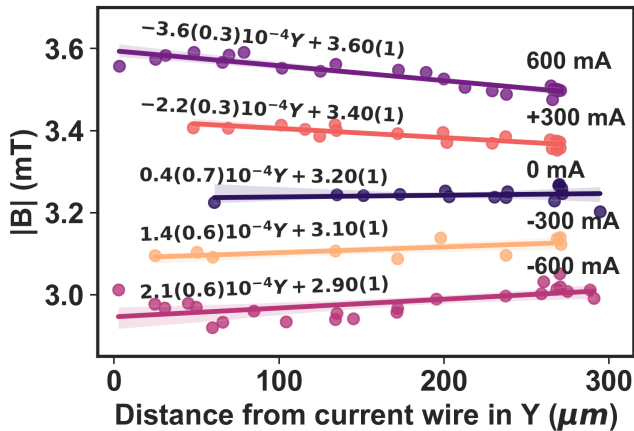


Fig. 4. The magnetic field strength plotted as a function of distance from the current wire in Y direction for different curve values. The colored solid lines are the linear-fit to the data and the shaded area show the 95 % confidence bounds.

Shown in Fig. 4 is the total magnetic field strength estimated from the ODMR spectrum of diamond NV crystals that are spatially scattered across the FOV for different current intensities. The B-field values are plotted as a function of the distance from the current-carrying

wire. As expected, it is evident from the estimation that the higher the current value, the greater the magnetic field. The bias field (0 mA) alone with zero current in the wire is shown as a reference. A small total magnetic field gradient of $0.1 \text{ mT}/300 \mu\text{m}$ is observed in the y direction. However, no gradient was observed for lower current values. Fluctuations in the values of the total magnetic field strength are attributed to the magnetic noise induced in the measuring environment. The effect is more pronounced at higher currents, probably caused by the crosstalk between the MW strip lines or by the heating of the wire due to the high DC current.

IV. CONCLUSIONS AND OUTLOOK

In this paper, we proposed a wide-field diamond NV magnetometer in arbitrarily oriented $1 \mu\text{m}$ diamond powder capable of simultaneously measuring the spatially varying DC magnetic fields over large fields of view ($> 300 \mu\text{m}$). As a general demonstration, we employed this NV sensor to measure the magnetic field generated by a current-carrying wire. Our experimental results show that the measured magnetic field value with an NV sensor for a given current intensity is in good approximation to the theoretically estimated value. However, the current wide-field setup limits the ability to map the magnetic-field distribution at all spatial points with high resolution. Additionally, the magnetometer applicability might be limited as a result of the limited number of micro-diamonds that are oriented arbitrarily to the applied magnetic field. Further improvements are foreseen that could improve the resolution and B-field sensitivity. For example, the sensitivity could be improved by using pulsed ODMR techniques and a high-NA objective. Additionally, we reconstructed the vector magnetic fields relative to the diamond reference frame. In the future, a follow-up work is planned to implement absolute vector magnetometry using arbitrarily oriented diamond powder by calibrating the NV orientation specific to the applied magnetic field direction with 3D Helmholtz coils. Our initial experimental results highlight the possibility of vector magnetometry using arbitrarily oriented diamond crystals.

V. ACKNOWLEDGMENTS

The research was carried out within the TEAM NET programme of the Foundation for Polish Science co-financed by the European Union under the European Regional Development Fund, project POIR.04.04.00-00-1644/18.

-
- * saravanan.sengottuvel@doctoral.uj.edu.pl
- [1] D. Le Sage, K. Arai, D. R. Glenn, S. J. DeVience, L. M. Pham, L. Rahn-Lee, M. D. Lukin, A. Yacoby, A. Komeili, and R. L. Walsworth, *Nature* **496**, 486 (2013).
 - [2] F. Casola, T. van der Sar, and A. Yacoby, *Nat. Rev. Mater.* **3** (2018), [10.1038/natrevmats.2017.88](https://doi.org/10.1038/natrevmats.2017.88).
 - [3] D. Vasyukov, Y. Anahory, L. Embon, D. Halbertal, J. Cuppens, L. Neeman, A. Finkler, Y. Segev, Y. Myasoedov, M. L. Rappaport, M. E. Huber, and E. Zeldov, *Nat. Nanotechnol* **8**, 639 (2013).
 - [4] P. Ripka, *Sensors and Actuators A: Physical* **33**, 129 (1992).
 - [5] H. Dehmelt, *Physical Review* **105**, 1487 (1957).
 - [6] W. Bell and A. Bloom, *Physical Review* **107**, 1559 (1957).
 - [7] E. D. Herbschleb, H. Kato, Y. Maruyama, T. Danjo, T. Makino, S. Yamasaki, I. Ohki, K. Hayashi, H. Morishita, M. Fujiwara, and N. Mizuochi, *Nat. Commun.* **10** (2019), [10.1038/s41467-019-11776-8](https://doi.org/10.1038/s41467-019-11776-8).
 - [8] G. Balasubramanian, P. Neumann, D. Twitchen, M. Markham, R. Kolesov, N. Mizuochi, J. Isoya, J. Achard, J. Beck, J. Tissler, V. Jacques, P. R. Hemmer, F. Jelezko, and J. Wrachtrup, *Nat. Mater.* **8**, 383 (2009).
 - [9] J. M. Taylor, P. Cappellaro, L. Childress, L. Jiang, D. Budker, P. R. Hemmer, A. Yacoby, R. Walsworth, and M. D. Lukin, *Nature Physics* (2008), [10.1038/nphys1075](https://doi.org/10.1038/nphys1075), [arXiv:0805.1367](https://arxiv.org/abs/0805.1367).
 - [10] F. Dolde, H. Fedder, M. W. Doherty, T. Noebauer, F. Rempp, G. Balasubramanian, T. Wolf, F. Reinhard, L. C. L. Hollenberg, F. Jelezko, and J. Wrachtrup, *Nat. Phys* **7**, 459 (2011).
 - [11] V. M. Acosta, E. Bauch, M. P. Ledbetter, A. Waxman, L.-S. Bouchard, and D. Budker, *Phys. Rev. Lett.* **104**, 070801 (2010).
 - [12] M. W. Doherty, V. V. Struzhkin, D. A. Simpson, L. P. McGuinness, Y. Meng, A. Stacey, T. J. Karle, R. J. Hemley, N. B. Manson, L. C. L. Hollenberg, and S. Prawer, *Phys. Rev. Lett.* **112**, 047601 (2014).
 - [13] D. Le Sage, L. M. Pham, N. Bar-Gill, C. Belthangady, M. D. Lukin, A. Yacoby, and R. L. Walsworth, *Phys. Rev. B* **85**, 121202 (2012).
 - [14] P. Maletinsky, S. Hong, M. S. Grinolds, B. Hausmann, M. D. Lukin, R. L. Walsworth, M. Loncar, and A. Yacoby, *Nat. Nanotechnol* **7**, 320 (2012).
 - [15] K. Jensen, V. M. Acosta, A. Jarmola, and D. Budker, *Phys. Rev. B* **87**, 014115 (2013).
 - [16] D. A. Redman, S. Brown, R. H. Sands, and S. C. Rand, *Phys. Rev. Lett.* **67**, 3420 (1991).
 - [17] N. B. Manson, J. P. Harrison, and M. J. Sellars, *Phys. Rev. B* **74**, 104303 (2006).
 - [18] F. Jelezko, T. Gaebel, I. Popa, A. Gruber, and J. Wrachtrup, *Phys. Rev. Lett.* **92**, 076401 (2004).
 - [19] J. R. Maze, P. L. Stanwix, J. S. Hodges, S. Hong, J. M. Taylor, P. Cappellaro, L. Jiang, M. V. G. Dutt, E. Togan, A. S. Zibrov, A. Yacoby, R. L. Walsworth, and M. D. Lukin, *Nature* **455**, 644 (2008).
 - [20] J. Wrachtrup, C. Vonborczyskowski, J. Bernard, M. Orrit, and R. Brown, *Nature* **363**, 244 (1993).
 - [21] S. Steinert, F. Dolde, P. Neumann, A. Aird, B. Naydenov, G. Balasubramanian, F. Jelezko, and J. Wrachtrup, *Rev. Sci. Instrum.* **81**, 043705 (2010), <https://doi.org/10.1063/1.3385689>.
 - [22] L. M. Pham, D. Le Sage, P. L. Stanwix, T. K. Yeung, D. Glenn, A. Trifonov, P. Cappellaro, P. R. Hemmer, M. D. Lukin, H. Park, A. Yacoby, and R. L. Walsworth, *New Journal of Physics* **13**, 045021 (2011), [arXiv:1207.3339](https://arxiv.org/abs/1207.3339).
 - [23] M. Chipaux, A. Tallaire, J. Achard, S. Pezzagna, J. Meijer, V. Jacques, J.-F. Roch, and T. Debuisschert, *Eur. Phys. J. D* **69**, 166 (2015), [arXiv:1410.0178](https://arxiv.org/abs/1410.0178).
 - [24] D. Maskowicz, R. Jendrzewski, W. Kopec, M. Gazda, J. Karczewski, P. Niedzialkowski, A. Kleibert, C. A. F. Vaz, Y. Garcia, and M. Sawczak, *Materials* **14** (2021), [10.3390/ma14237135](https://doi.org/10.3390/ma14237135).
 - [25] M. Mrózek, J. Młynarczyk, D. S. Rudnicki, and W. Gawlik, *Appl. Phys. Lett.* **107**, 013505 (2015), <https://doi.org/10.1063/1.4923252>.
 - [26] M. Ficek, M. J. Głowacki, K. Gajewski, P. Kunicki, E. Gacka, K. Sycz, M. Mrózek, A. M. Wojciechowski, T. P. Gotszalk, W. Gawlik, and R. Bogdanowicz, *Coatings* **11** (2021), [10.3390/coatings11111332](https://doi.org/10.3390/coatings11111332).
 - [27] MATLAB, *version 9.9 (R2020b)* (The MathWorks Inc., Natick, Massachusetts, 2020).